Automated robust test framework for electrical impedance tomography

Pascal O. Gaggero[1], Andy Adler[2], Andreas D. Waldmann[3], Yasin Mamatjan[2,4], Jörn Justiz[1] and Volker M. Koch[1]

[1]Institute for Human Centered Engineering, Bern University of Applied Sciences, Biel/Bienne, Switzerland
[2]System and Computer Engineering, Carleton University, Ottawa, ON K1S 5B6, Canada
[3]Swisstom AG, Landquart, Switzerland
[4]Department of Electrical-Electronics Engineering, Zirve University, Gaziantep, Turkey

E-mail: pascal@gaggero.ch, adler@sce.carleton.ca, awa@swisstom.com, mamatjan.yasin@zirve.edu.tr, joern.justiz@bfh.ch, volker.koch@bfh.ch

Abstract. An automated test system and procedure is proposed, designed to enable systematic testing of electrical impedance tomography (EIT) devices. The system is designed to calculate reliable, repeatable and accurate performance figures of merit of an EIT system using a saline phantom and industrial robot arm. Applications of the test system are to compare EIT devices against requirements, or to help optimize a device for its operating parameters. A test methodology and sample test results are presented to illustrate its use. The system is used to compare image quality and contrast detection for a range of stimulation and measurement patterns, and results show the best images when the pair of current injection electrodes is spaced between 45 and 170 degrees on a tank. Finally, we propose a classification of the object detection errors, which can facilitate comparison of EIT instrument specifications.

Keywords: EIT, test system, robot, forward model, image quality

PACS numbers:

AMS classification scheme numbers:

Submitted to: *Physiol. Meas.*

1. Introduction

Electrical impedance tomography (EIT) is an imaging technique, which uses body surface electrodes to inject small alternating electrical currents and measure the resulting potential fields. Using these measurement, an image of the spatial distribution of impedance within the body is reconstructed. EIT does not use ionizing radiation, and offers the advantage of an ability to continuously monitor a body without bulky instrumentation. Today's main biomedical application of EIT is lung monitoring. The therapeutic goal is to be able to better apply lung protective ventilation techniques, which require the knowledge of the spatial distribution of air (inferred from the spatial distribution of the electrical impedance) within the lungs in real-time. Recent tests in animals show EIT-guided ventilation can improve respiratory mechanics and gas exchange, while reducing ventilator induced lung injury [1]. From the user's perspective, the value of an EIT system is in its ability to provide clinically useful data on a patient's status. This means that the various components of such a system (electrodes, electronics hardware, and reconstruction algorithms) need to be designed and calibrated to optimize this clinical utility. As EIT systems move from the lab toward manufacture, it is increasingly important to develop approaches to evaluate (and optimize) their system performance. Such evaluation requires a robust framework to measure and quantify the behavior of the EIT system from the conductivity change in the relevant regions of interest to the assessment of parameters of image accuracy. Such performance assessment serves two goals: it can determine the reliability with which a given EIT system can measure specific clinical parameters; and, it can help optimize an EIT system by testing the overall effect of design changes.

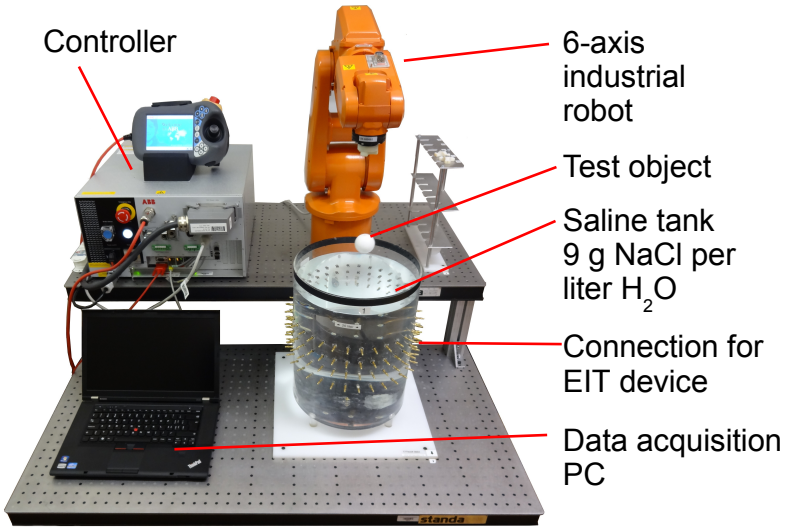

Figure 1. Automated test system for a medical EIT device including a 6-axis industrial robot, a tank (phantom) filled with saline and the test object, here a sphere of non-conductive material.

Numerous studies have been published on EIT performance evaluation. A first method consists in using simulation models [2, 3]. This method has the disadvantage

that simulations only take into account the known modeled behavior. A second category of methods uses solid-state resistors mounted on printed circuit boards, forming more or less complex meshes, has been proposed by many authors [4–8]. Such resistor phantoms have the advantage of stability and exactly known properties; however, they have a limited ability to model the behavior of EIT as a functional imaging modality, which should have the ability to create feasible conductivity changes at arbitrary locations. Instead, contrasting changes in resistor phantoms are typically limited to a small number of specific resistor locations. Furthermore, changes in a single resistance will generally correspond to an anisotropic perturbation in the corresponding model, which will typically not correspond to physical impedance contrasts [9, 10]. Other types of test models which approximate the real clinical conditions better are saline tanks. An EIT system which is connected to a saline tank experiences realistic electrical load (ionic interface, stray capacitance and realistic impedance load for current source), and more importantly the EIT signal generated with such a set-up results from the flow in three dimensions of a current in a physical test body of a size close to the clinic case. A saline tank phantom is able to generate signals which correspond more closely to application requirements, such as "a change of 50 ml of air in a cylindrical volume". In medical term this corresponds to a precisely located change of the lung's volume. Tanks are filled with a conductive solution, typically between 0.1 S/m and 2 S/m. From a modeling perspective, a saline phantom has the advantage over FEM- and resistor-based phantoms in that it accounts for imperfections in the electronics hardware and electrode interface. In the saline phantoms, solid state test objects are being used to create impedance contrasts. In this context a system that would be able to automatically position test objects within the tank would help characterizing EIT system better by providing advanced screening availability. For this reason, Yasin *et al.,* [11] proposed the use of a custom built Lego based xyz gantry positioning device to place test objects within a saline phantom. We have identified some issues with this system, which limits its use for the type of system baseline testing we envision. Specifically, it suffers from a lack of mechanical stability, and requires regular calibration, which makes it not well suited for long test protocols.

Complete assessment and optimization of EIT system performance is important. Using saline tanks one can generate realistic test signals. However, it is still not possible to make a robust saline tank test regarding system calibration, repeatability and reliability. Thus for overall EIT system assessment, the following requirements were identified: 1) end-to-end evaluation, 2) stable, repeatable system, 3) performance metrics relevant to clinical parameters. Thus, in this paper, we describe a system and evaluation framework which is able to perform reliable and accurate evaluation of EIT systems. Specifically, we make the following contributions 1) an automatized framework to make robust and repeatable measurements, 2) improvements on the position accuracy, position precision and resolution metrics and 3) tentative classification of the measured error in classes.

2. Methods

2.1. Overview

An overview of the developed test framework is depicted in Figure 1 (picture) and Figure 2 (schematic diagram). All the subsystems were centrally orchestrated by a

personal computer (PC). The key subsystem was the robotic arm that placed the test object within the phantom filled with saline water. The use of this industrial grade robot allowed us to fulfill our requirement of stability and repeatability. The test object was placed at well-defined positions according to a predefined measurement protocol, see Figure 3, and the EIT data were recorded for each position. The test protocols were saved into text files that were interpreted by the PC to execute the test instructions. The same measurement protocol can be repeated using various sets of test parameters, for example different settings of the EIT instrument. At the end, one obtains a collection of measurements related to the test parameters. The EIT data can be recorded according to three use cases: A) as raw voltage data, B) and B') as pixilated images (see Figure 4 and Section 2.5 for details). In all cases, the produced images are analyzed using the developed image metrics, which compared the difference between the ground truth position, shape and size of the test object with the same parameters measurement on the EIT image.

We designed the test system to make it easy for a manufacturer to interface their EIT instrument to it using standard 4 mm connectors. We aimed at developing a standardized test protocol which would enable fair comparison between systems and cross-validation of hardware performance between manufactures. Moreover, we designed the system such that the calibration protocol can be certified and made traceable using national norms at reasonable costs.

In this paper, we tested two sample test parameters to illustrate our method: 1) the current injection angle (offset) and 2) the reconstruction hyper parameter. Thus the expected results are recommendation concerning the best choice of those parameters for EIT measurement with the tested system.

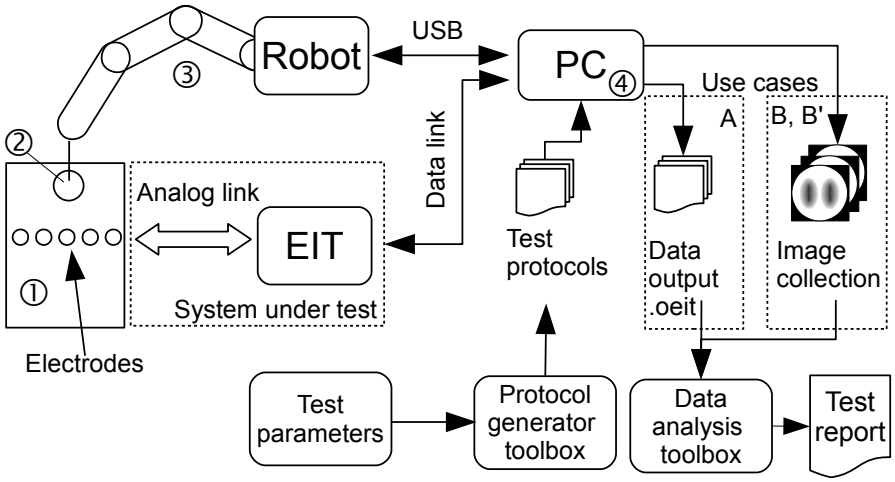

Figure 2. Schematic representation of the automated test syste

2.2. Robotic test system

The data acquisition system, see Figure 2, was composed of: ① a saline phantom, ② test objects, ③ an industrial 6-axis robotic arm and ④ a personal computer (PC). The industrial 6-axis robotic arm IRB 120 from ABB (Baden, Switzerland) placed calibrated test objects at different positions with a repeatability of ± 0.02 mm in

the saline phantom. The robot has six degrees of freedom and is designed to carry a weight of 1 kg at maximal extension. The workspace of the robot allows placing the test objects at any position within the phantom as well as taking the test objects completely out of the saline solution. The robot is driven by a controller "IRC5 Compact controller" and programmed using the programing language RAPID proper to ABB robots. The automation of the object placement allowed us to provide precise, accurate and reproducible measurements while minimizing human errors. Since no human action was required during the data acquisition one can acquire a high density of data points even if it requires several measurement hours.

The saline phantom is composed of a cylindrical tank filled with a saline solution. This phantom, produced by the Centre Suisse d'Electronique et Microtechnique (Landquart, Switzerland), is used to emulate a simplified adult human thorax and is composed of an acrylic glass cylinder with an internal diameter of 290 mm and a height of 375 mm. Four rows of a total of 128 standard 4 mm gold-platted connectors allow versatile device connections including snap-on ECG cables. An additional pin at the center of the tank bottom can be used by EIT devices that use an additional ground electrode. In the sample results presented in this paper, we used only one single row of 32 electrodes. The phantom was filled with a solution composed of 22 l of water and 198 g of NaCl (i.e., conductivity of the solution was about 1.6 S/m). We observed that to ensure stable conditions and a homogenous conductivity distribution, the first measurements were required to be made earliest 12 h after mixing (this value depends on the environmental conditions and requires to be experimentally determined). This was mainly due to the time required for the fresh tape water to reach room temperature and for the dissolved gases, produced when the water was poured, to quit the solution. Ball-shaped test objects with diameter of 25 mm (about 10 ml, model G9a25.0.D) and 45 mm (about 50 ml, model G9A45.0.V) manufactured by KGM Kugelfabrik (Fulda, Germany) are available to generate impedance changes in the saline phantom. The material used for the balls is polyoxymethylene (POM). It has a resistivity value much greater than 1 G$\Omega \cdot$ m. The selected volumes of 10 ml and 50 ml were chosen in relation with the physiological functions of the lung. The 10 ml ball and 50 ml ball represents 1/50 and 1/10 of the tidal volume (TV) of an adult person (500 ml [12]), respectively. In this paper, we only made use of the 50 ml object. The test object has a M5 thread, which is available for fixation purposes. For this project, we fixed the object using a fine fishing line thread. The influence of the line on the impedance measurements can be neglected. The advantage of a spherical target is that it is rotationally symmetric, which simplifies positioning and subsequent analysis; however, it is a straightforward extension to equip the system with and other kind of target.

2.3. Sample EIT system under test

The EIT system under test was a technical preview of the Pioneer Set, version August 2012, from Swisstom AG (Landquart, Switzerland). This system has 32 active electrodes and can inject up to 10 mA from 50 kHz to 250 kHz, see [13]. This system has the advantage that one can configure the current injection and voltage measurement patterns. In this work, we call "offset" the number of electrodes between the injection or measurement pair. Thus an adjacent pattern is defined by setting the offset parameter to 0 and an opposite pattern with an offset 15. In the present experimental set-up, the N=32 electrodes were distributed uniformly around the cylinder-shaped tank, thus offsets 0 to 15 also correspond to injection angles from

11.25 to 180 degree, respectively. In this article, the current injection angle (offset) and voltage measurement angle were always equal. If the electrodes are not uniformly distributed or if tank shape is not cylindrical, then the measured values would depend on the position as well as the injection angle. This implies that the choice of a round shaped tank allows for a better decoupling of the effects of each current injection angle. For the measurement a fix current amplitude of 1 mA with a frequency of 100 kHz was selected. During the data acquisition phase all 32 by 32 measurement were acquired, based on the EIT hardware used. Then for the image reconstruction, done in post-processing, we only selected the measurements which did not use a current-stimulation electrode (four-point measurement scheme). In general, in a complete set of pair measurements for pair drive (with the same offset pattern) there are three which use a current-stimulation electrode. This yields the N(N-3)=928 measurements in a frame. When using opposite patterns for stimulation and measurement, there are only two measurements which use current-stimulation electrodes, which yields Nx(N-2) = 960 measurements per frame.

2.4. Sample test protocol

We used a sample test protocol, which placed the test object on a 200 mm (x-direction) by 180 mm (z-direction) grid, using 21 by 21 equally spaced test points. Since we were doing difference imaging, it was necessary to acquire a reference image, which we selected to be the phantom without any test object inside. In Figure 3, the position of the test object during a reference cycle is marked by a circled "r". Since the test object was attached using a thin thread after each horizontal translation (xy-plane), it was necessary to wait about 30 s before the object was stabilized. Therefore the used column-wise data acquisition protocol minimized the horizontal displacements. At the beginning, between each column and at the end of the protocol a reference data set was acquired. This allowed us to minimize the effects of the instrumentation drift, not presented here, which was measured to be in average (2 µV / h). This undesirable effect can be mitigated by taking a new reference at regular intervals, in this case every 10 minutes. For each position, 100 images or data frames were acquired at a frame rate of 10 images per second.

2.5. Developed image metrics

We used and extended the image quality figures of merit developed for the GREIT algorithm [14] to assess the performance of reconstruction algorithms. From the original implementation, we identified some shortcomings: 1) the original implementation does not propose a solution to deal with multiple detected objects (defined as pixel-wise amplitude value larger than 25 % of maximum), 2) the resolution metric postulates that the test object has the size of a point and 3) it is not clear how to deal with the time fluctuation of the data (i.e., the noise) for example for the position error metric. The novelties of the proposed approach are 1) the image prepossessing steps to precisely isolate the test object within the image (see Figure 5), 2) the distinction between position accuracy and precision, and 3) the introduction of a correction factor for the object size in the calculation of the resolution. The image quality criteria developed in this article were based on the knowledge of the ground truth value, which was easily accessible since size, shape and position of the test object are known. Image reconstruction used a Gauss-Newton solver, with a

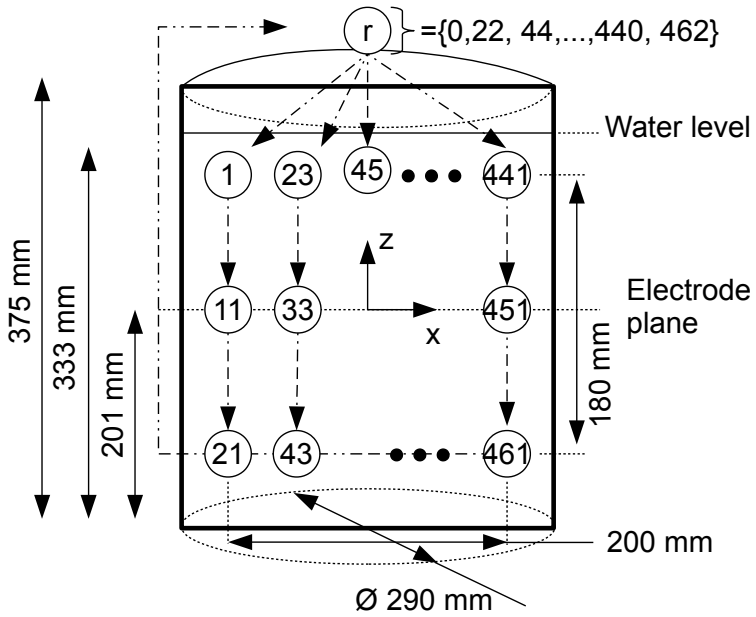

Figure 3. Vertical cross-section view of the saline phantom. The tank when filled up to the "water level" mark contains 22 liters of solution. The test positions with the target inside the saline solution are numbered from 1 to 461. A new reference image, with the target object outside the saline solution, was acquired before and after each column-wise scan (i.e., 0, 22, 44, ..., 440 and 462). Thus a total of 463 measurement points including the reference images were acquired.

spatial high pass prior [15] and compensation for electrode movement [16]. The hyperparameter, as defined in the algorithm proposed by Adler *et al.,* value was chosen heuristically to deliver a visually good compromise between resolution and noise performance. We used the EIDORS software package [17] implemented in Matlab (Natick, Massachusetts, USA) to calculated our reconstruction matrices. However, the proposed methods are similarly applicable to all reconstruction algorithms that output a pixel-based image.

In this work, we distinguished three use cases A, B and B'; they are depicted in Figure 4 with their associated data processing flow chart. In case A, voltage data, $\mathbf{y}$, were recorded and the image reconstruction was done during post-processing using EIDORS. In case B, the EIT instrument delivers ready-to-use differential images. This method requires a "reference trigger" signal that triggers the reference taking mechanism of the EIT system. In case B', the EIT instrument sends pre-calculated "images" of the form $\mathbf{X} = \mathbf{R}\mathbf{y}$, where $\mathbf{y}$ is defined as the voltage values measured by the EIT system and $\mathbf{R}$ is the reconstruction matrix. The reference image, $\mathbf{X}'_{\mathrm{ref}} = \mathbf{R}\mathbf{y}_{\mathrm{ref}}$, needs to be selected during post-processing. To get the differential EIT image, $\mathbf{X}$, one then needs to calculate $\mathbf{X} = \mathbf{X}' - \mathbf{X}'_{\mathrm{ref}}$. For linear reconstruction algorithms, cases B and B' are equivalent. Nevertheless, we keep the distinction between both cases in order to accommodate for both EIT hardware configurations. This subdivision in distinct cases A, B and B' has been designed such that the data processing chain and the system under test are better defined. Use case A is more suited for tests on the raw data (for example using EIDORS for the reconstruction) and use cases B and B'

are more suited to test the instrumentation as a whole including image reconstruction. For the sample results, presented in this paper we selected case A.

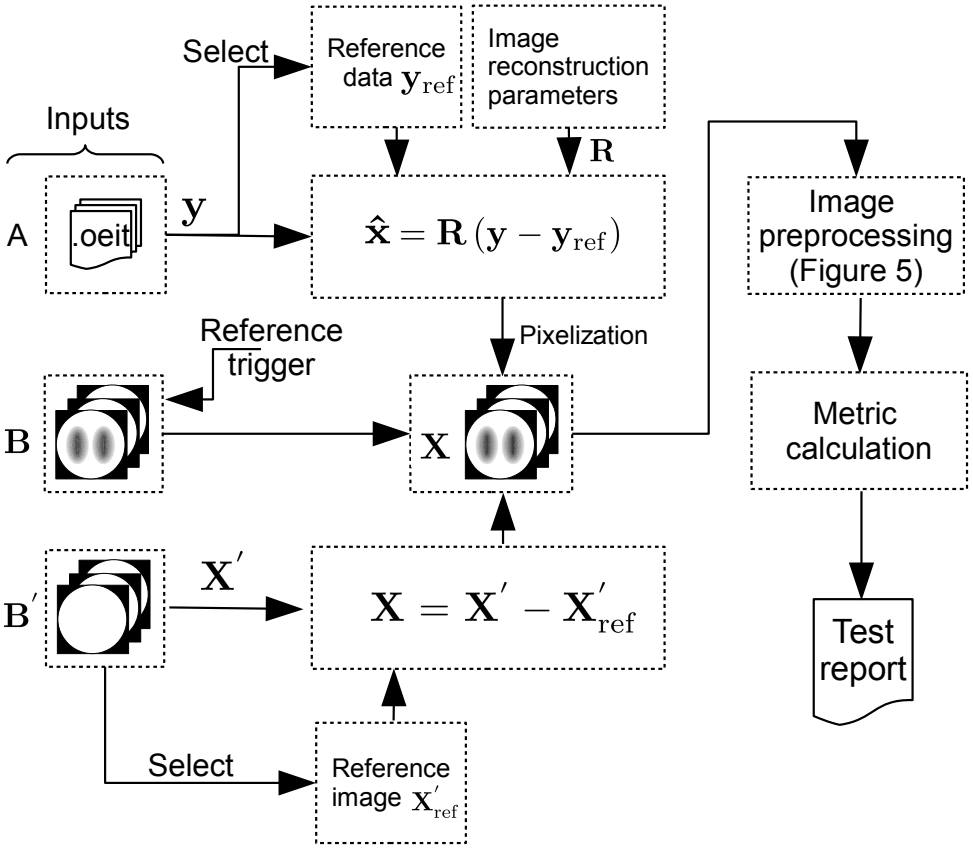

Figure 4. Schematic representation of the three use cases A, B and B', where $\hat{\mathbf{x}}$, a vector of size $1 \times N_{\mathrm{node}}$, is the reconstructed conductivity distribution, $\mathbf{R}$, a matrix of size $N_{\mathrm{ch}} \times N_{\mathrm{node}}$, is the reconstruction matrix and $\mathbf{y}$, a vector of size $1 \times N_{\mathrm{ch}}$, are the differential voltage measurements. N_{ch} and N_{node} are the number of measurement channels and the number of element of the finite elements mesh model, respectively. To make an image, $\hat{\mathbf{x}}$ is mapped on a pixel grid of size $N_{\mathrm{pixel}} \times N_{\mathrm{pixel}}$ (i.e. "pixelization"). In this paper, we set $N_{\mathrm{pixel}} = 64$. $\mathbf{X}'$is a matrix of size $N_{\mathrm{pixel}} \times N_{\mathrm{pixel}}$ which is the non-differential EIT image. $\mathbf{X}$ is a matrix of size $N_{\mathrm{pixel}} \times N_{\mathrm{pixel}}$ which is the differential EIT image.

After the reconstructed image $\mathbf{X}$ had been obtained, four preparatory steps represented in Figure 5 were required: 1) The first step was to compensate for the sign of the impedance change, such that if the object was expected to be of negative value the image, $\mathbf{X}$, needed to be multiplied by -1. This sign compensated image is named $\mathbf{X}_{\mathrm{sc}}$. One can also note that the pixels outside the medium were given the value zero. 2) Then a threshold was applied. This step turned the image into a binary image called $\mathbf{X}_{\mathrm{t}}$. We selected the value of the threshold at 25% of the image's maximal value, as proposed by Adler *et al.,* [14]. 3) Due to reconstruction artifacts and noise it was possible that after step 2 several distinct regions were found in the

image. Thus, in order to select the one which corresponded to the test object, we needed to apply a discrimination algorithm. We used a labeling of disjoint regions in the image (using the approach of [18]). In this work, we assume that the region with the largest intensity was the object (sum of all pixel values within the region). The image resulting of the whole process is named $\mathbf{X}_{\mathrm{la}}$, and corresponds to the detected object on the image. Thus, we can also apply $\mathbf{X}_{\mathrm{la}}$ as a mask on $\mathbf{X}_{\mathrm{sc}}$ (i.e., multiply each element of $\mathbf{X}_{\mathrm{la}}$ with each element of $\mathbf{X}_{\mathrm{sc}}$) to obtain the image in the region of interest (ROI) and zero everywhere else. This new matrix was called $\mathbf{X}_{\mathrm{lasc}}$. 4) An equivalent idealized test-object like shaped (in this case round) test object image with the same surface and position as the detected one can be calculated.

The proposed image-based metric implicitly includes the performance not only from the hardware or the collected data but also from the reconstruction algorithm and its different parameters, which is a desired feature, because we would like to test the instrument as a whole.

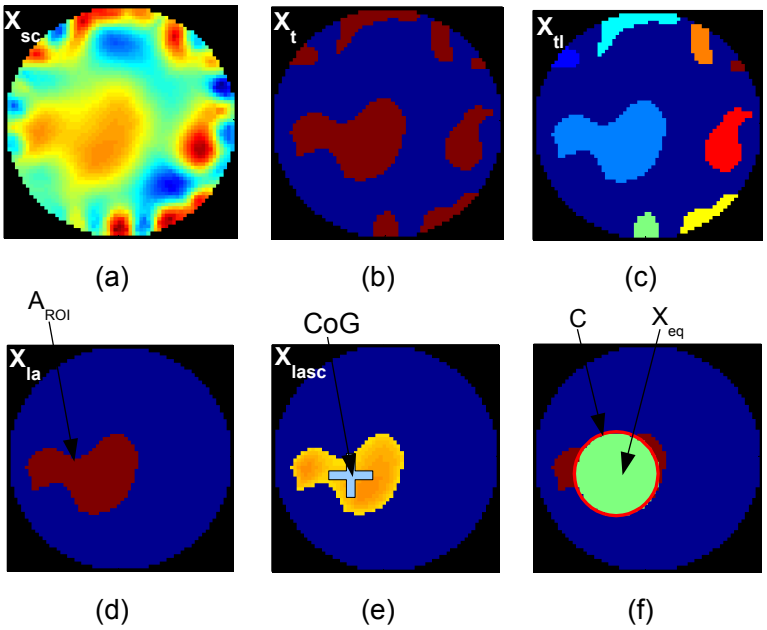

Figure 5. Preparatory steps and image processing required for the calculation of the image metrics. Note that for this figure we selected a particularly bad image for a better illustration of the processing steps. (a) sign compensated reconstructed image, (b) threshold image at 25 % of the maximum, (c) labeled image where each color corresponds to an independent region, (d) image of the footprint of the detected object, (e) extracted image of the detected object. The center of gravity (CoG) is given by the cross, (f) $\mathbf{X}_{\mathrm{eq}}$ is the ideal round-shaped image of the test object with the surface and position matching the one measured in (d). The circle C delimits the ideal test object.

Position accuracy (PA) is the distance between the center of gravity (CoG) of the object placed into the test medium and the measured CoG of the imaged object

after image reconstruction and averaging, see Figure 6. CoG is calculated as follow:

$$C_{\text{cogx}} = \frac{\sum_{i=1}^{N_{pixel}} \sum_{j=1}^{N_{pixel}} [X_{\text{lasc}}]_{i,j} [C_x]_{i,j}}{\sum_{i=1}^{N_{pixel}} \sum_{j=1}^{N_{pixel}} [X_{\text{lasc}}]_{i,j}} \tag{1}$$

$$C_{\text{cogy}} = \frac{\sum_{i=1}^{N_{pixel}} \sum_{j=1}^{N_{pixel}} [X_{\text{lasc}}]_{i,j} [C_y]_{i,j}}{\sum_{i=1}^{N_{pixel}} \sum_{j=1}^{N_{pixel}} [X_{\text{lasc}}]_{i,j}} \tag{2}$$

where $[C_{\text{x}}]_{i,j}$ and $[C_{\text{y}}]_{i,j}$are the x and y coordinate of the (i, j) pixel, respectively. C_{x} and C_{y} are N_{pixel} x N_{pixel} matrices, where each value is the x and respectively the y coordinate of the center of each corresponding pixels in the reconstructed image with respect to the tank center. N_{pixel} is the size of the image. In this work the size of the image is set to 64 pixels by 64 pixels. The coordinates are given in normal units where the tank radius is equal to 1. The same operation is repeated for a collection of images of the same situation, from which the mean position $(\overline{C_{\text{cogx}}}, \overline{C_{\text{cogy}}})$ is calculated. In this work, we only consider two-dimensional reconstructions, thus the calculated CoGs do corresponded to the projection in the electrode plane of the true three-dimensional position. Nevertheless an extension of this work in three dimension is possible. We recommend selection of a number of samples, N_m, such that the confidence interval on the estimated mean reach at least 95%. In this work, we estimated that $N_m = 100$ samples was sufficient. The position accuracy relative to the true position of the test object is given by:

$$M_{\text{PA}} = \sqrt{\left(C_{\text{setx}} - \overline{C_{\text{cogx}}}\right)^2 + \left(C_{\text{sety}} - \overline{C_{\text{cogy}}}\right)^2} \tag{3}$$

where C_{setx} and C_{sety} contain the true position coordinates for the object.

Position Precision (PP) is the standard deviation from the mean of the measured positions:

$$C_{\text{sdtx}} = \sqrt{\frac{1}{N_m} \sum_{i=1}^{N_m} \left(C_{\text{cogx},i} - \overline{C_{\text{cogx}}}\right)^2} \tag{4}$$

$$C_{\text{sdty}} = \sqrt{\frac{1}{N_m} \sum_{i=1}^{N_m} \left(C_{\text{cogy},i} - \overline{C_{\text{cogy}}}\right)^2} \tag{5}$$

where $C_{\text{cogx},i}$ and $C_{\text{cogy},i}$ represents the CoG coordinates of the i-th image and N_m is the number of acquired measurement sample. The position precision is given by:

$$M_{\text{PP}} = \sqrt{C_{\text{sdtx}}^2 + C_{\text{sdty}}^2} \tag{6}$$

Such distinction between precision and accuracy could be made for all the other metrics as well. We implemented the two next metrics, resolution and deformation as the average over time for each position ("accuracy"). In other words, it corresponded to an estimate of the resolution and deformation, that we would get if the noise was equal to zero. This choice is motivated by the fact that both metrics were designed to investigate static errors due to the image reconstruction algorithm and geometrical errors.

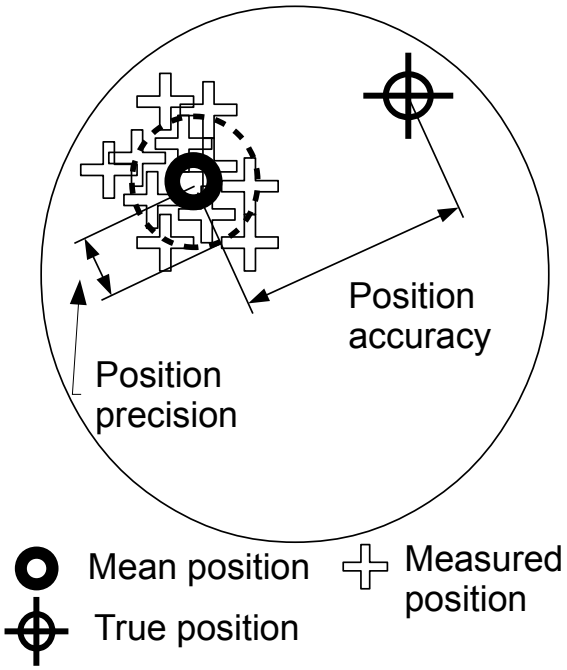

Figure 6. The position accuracy is given by the distance between the mean measured position and the true position. The position precision is given by the position standard deviation from the measured mean position.

Resolution (res) is a measure almost equivalent to the measurement of the point spread function (PSF) but corrected for the expected area. For the resolution one gets:

$$M_{\text{res}} = \sqrt{\frac{A_{\text{ROI}} - A_{\text{set}}}{A_0}} \tag{7}$$

where A_0 is the area of the cross-section of the tank given by $A_0 = r_{\text{tank}}^2 \pi$, A_{ROI} is the area of the detected object and A_{set} is the cross section area of the true test object. The square root is taken so that resolution is represented as a linear distance, rather than an area. In EIT the PSF is not uniformly spatially distributed (i.e. non-shift invariant) thus a large test object may be affected by this. To avoid this situation, we recommend to select A_{set} such that it is small enough compared to A_0.

Deformation (def) is a measure for how much the imaged object A_{ROI} resembles a disk of identical surface X_{eq}. In a case where the ideal shape of the reconstructed object is not a disk, the previous equation should be reformulated accordingly. For this purpose the ratio of number of pixels outside the equivalent disk and the total number of pixels of the ROI is calculated, see Figure 5 (f).

$$M_{\text{def}} = \frac{\sum\limits_{[X_{\text{la}}] \in !C} [X_{\text{la}}]_{i,j}}{\sum_{i=1}^{N_{pixel}} \sum_{j=1}^{N_{pixel}} [X_{\text{la}}]_{i,j}} \tag{8}$$

where the sum over $[X_{\text{la}}] \in !C$ designate all the element outside the circle C. The

choice of a disk as the comparison shape corresponds to the ideal projection of the spherical target object on the electrode plane.

Z-score is a measure of the signal quality before any image reconstruction steps. The z-score is expressed as the ratio of the norm of the measured voltages over the standard deviation of the noise, see Adler *et al.,* [19]. Gaggero *et al.,* [20] empirically established that a z-score value between 6 and 15 starts to produce a visible object on the screen for an image rate of 10 images per second. The z-score is calculated as follows. First, the mean of the signal in the time direction is calculated:

$$[\overline{y_{\mathrm{d}}}]_j = \frac{1}{N_{\mathrm{m}}} \sum_{i=1}^{N_{\mathrm{m}}} [y_{\mathrm{d}}]_{i,j} \quad \text{with } j = 1, 2, ..., N_{ch} \tag{9}$$

Secondly, we take the norm over all channels:

$$\|y\| = \sqrt{\sum_{j=1}^{N_{\mathrm{ch}}} \left([\overline{y_{\mathrm{d}}}]_j \right)^2} \tag{10}$$

where N_{ch} is the number of measurement channel, in this paper 928 and $[y_{\mathrm{d}}]$ the differential voltage data of size N_{ch} channel times N_{m} measurements per channel.

The overall standard deviation of the noise is estimated as the square root of the mean of the variance of the noise over each channel:

$$\overline{n} = \sqrt{\frac{1}{N_{\mathrm{ch}}} \sum_{j=1}^{N_{\mathrm{ch}}} \frac{1}{N_{\mathrm{m}}} \sum_{i=1}^{N_{\mathrm{m}}} \left([y]_{i,j} - [\overline{y}]_j \right)^2} \tag{11}$$

Finally we get the z-score:

$$M_{\mathrm{z}} = \frac{\|y\|}{\overline{n}} \tag{12}$$

As a general comment about the presented metric, one can say that their results depend on the experimental conditions, typically if the size ratio between the test object and the tank is modified, it directly influences the metric value. Thus for benchmarking well-defined geometries must be used.

In this work, we use the five metrics (position accuracy, position precision, resolution, deformation and z-score) which we considered most representative for the evaluation of the EIT system we used. Following the proposed methodology, other metrics can be defined and customize to accommodate the user needs. As an example, a metric for artifacts could be defined by taking the difference between image X_{tl} and X_{la} in Figure 5.

2.6. Ranking in error classes

The results of the metrics presented hereafter in Section 3.1 are difficult to intuitively interpret. Therefore, we introduced a tentative ranking concept that assigned grades to given performance, see Table 1. In this table, we expressed the error value in percentile, this should be interpreted as 1% error corresponding to 1% of the tank radius. This is possible since, we normalized all our criterion with the tank radius or surface and represented all the obtained result in term of linear distances.

Table 1. Proposed error ranking in classes. 0 is the lowest grade. 10 is the best grade.

Error value	Classes or grades			
	Accuracy	Precision	Deformation	Resolution
> 40 %	0	0	0	0
[40 %, 30 %[	1	1	1	1
[30 %, 20 %[	2	2	2	2
[20 %, 15 %[	3	3	3	3
[15 %, 10 %[	4	4	4	4
[10 %, 5 %[	5	5	5	5
[5 %, 1 %[	6	6	6	6
[1 %, 0.5 %[	7	7	7	7
[0.5 %, 0.1 %[	8	8	8	8
[0.1 %, 0.05 %[	9	9	9	9
[0.05 %, 0 %]	10	10	10	10

3. Sample Results

This section presents two sample short studies with which we intend to illustrate the possibility to use the developed test system to evaluate and optimize the performance of EIT systems. The first one analyzes the effect of the current injection offset on the position accuracy. The second one maps the z-score for in-plane and off-plane objects. Based on the presented sample results and the tests made during the development of those metrics, we propose an error class based ranking method, see Section 2.6.

3.1. The influence of the offset parameter

In this section, we show that the evaluation and optimization of an EIT system using the proposed test system is possible. For this we selected sample test parameters and image reconstruction methods to illustrates our work. This choice was based on popular methods and default settings available in EIDORS. For those tests, we selected a simple Gauss-Newton solver with Gaussian prior parametrized with 4 different hyperparameters (hp) 2, 0.2, 0.02 and 0.002. Additionally, we also used GREIT parametrized with noise figure (NF) equal to 0.5 (i.e., EIDORS' default configuration). The measurements were made at 10 images per second for a total of 10 seconds of data per test point. The analysis was simplified with the separation of the radius of the tank in 4 zones. Within a zone the measured metrics are averaged. Zone 1 from 100 mm to 90 mm corresponded to the area the closest to the electrodes. Zone 2 and 3 from 80 mm to 60 mm and 50 mm to 30 mm, respectively, corresponded to regions where the lungs are the most likely to appear. Finally, zone 4 from 20 mm to the center of the tank (0 mm). The position accuracy, in Figure 7, was around 0.1. One general important effect is that the position accuracy increased as the test object got closer to the tank's center. This effect was due to the preference of Gauss-Newton algorithm to place the reconstructed object in the center. GREIT seemed less affected by this effect and already exhibited very good accuracy in zone 1. The position precision got worse as the test object approached the tank's center, which was expected since the SNR represented by the z-score in Figure 8 also decreased. It can also be observed that according to Figure 8 the highest z-score value are reached with offset 15. But

offset 15, and to a lesser extent offset 14 and 13, performances are not good as shown on Figure 7. This effect can be explained by the loss of information content of the measurement for offset values higher than 12 because measurements at opposite (or nearly opposite) positions are nearly symmetric (with reversed current stimulation and measurement patters) and thus redundant. This effect can also be quantified using singular value methodology as presented by Gaggero *et al.*, [20]. Similar figures for deformation and resolution have also been calculated, the results were not presented here but the results were part of the Figure 10.

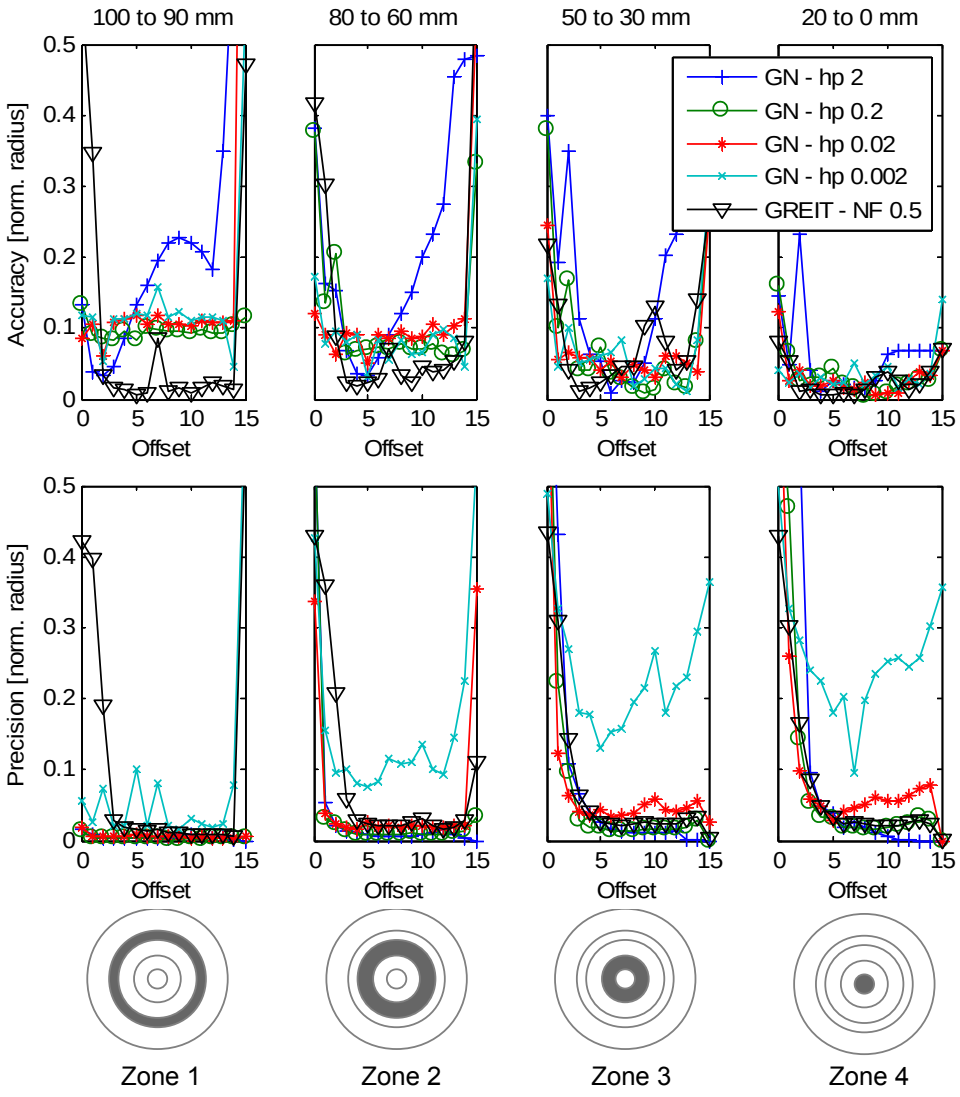

Figure 7. Position accuracy versus offset and position precision versus offset in the four zones. The tests were done using the following reconstruction parameters for the Gauss-Newton (GN) method hyper-parameters (hp) 2, 0.2, 0.02 and 0.002. and for the GREIT method noise figure (NF) 0.5. The zone positions given in the titles are calculated from the tank's center.

3.2. The influence of off-plane targets

In this section, we analyze how off-plane targets were imaged, see Figure 8. In practice, it is not always possible to place the electrodes (belt) at the same height as the region(s) of interest. For example, in lung monitoring application, the regions of interest are distributed in the z-direction. For an informed placement of the electrode belt, it is paramount to document the performances of the EIT instrument along the z-direction. The best performances were achieved when the object was exactly on the x-axis (i.e., at the electrode's plane). The z-score was the highest close to the electrode, then it decreased towards the center in all directions.

In Figure 9, we plotted the z-score against the position precision for all 441 tested positions in the xz-plane and for offsets ranging from 0 to 10. In this way, we generated data over a large range of SNR values. We did not selected the data using an offset ranging from 11 to 15 because for offset values larger than 10 outliers were seen in the results probably due to symmetry effects already observed by Gaggero *et al.,* [20]. The results depicted on Figure 9 showed a link between the position precision and the z-score. This link suggests that the z-score could be used as a possible real-time surrogate for the position precision, which measures the reliability of the target position in the image. Based on our results, we estimate that a threshold of 0.1 for position precision may be used to determine when an object can be seen in the EIT image. Using this threshold, we can measure in Figure 9 that a minimal z-score of 16 ensures that the object is seen on the image. Following this requirement, we can observe on Figure 8 that the object is visible in almost the whole measurement volume 200 mm by 180 mm starting from offset 4. This corresponded to the observed reconstructed images. The correlation between the z-score and the image precision parameters suggests that a real time indicator of the EIT image reliability based on the available real-time EIT raw voltage data can be developed.

3.3. Sample ranking of the errors

In this example, we selected all positions of the test object located on the electrode's plane. Then, the average over all metrics (position accuracy, position precision, deformation and resolution) using the error values in percent can be calculated, see Figure 10 (left). Alternatively and depending of the user's needs a weighted average could be used. Subsequently the calculated averages are categorized into error classes using Table 1. Note that result for deformation and resolution are not presented in this paper.

4. Conclusions

In this paper, we present an automated robust test framework based on a saline phantom data acquisition system for EIT. We introduced changes in the calculation of the GREIT image metric parameters to improve the original implementation. For example, the position error metric was also split into two distinct metrics, namely position accuracy and position precision. Position accuracy expressed the systematic error on the detected object's position. The position precision described the variation of the position with time due to the noise. This test system enabled us to perform parameter tuning procedures and tests on a sample EIT instrument. We also proposed a ranking of the metric results in classes which enabled easier comparison of the

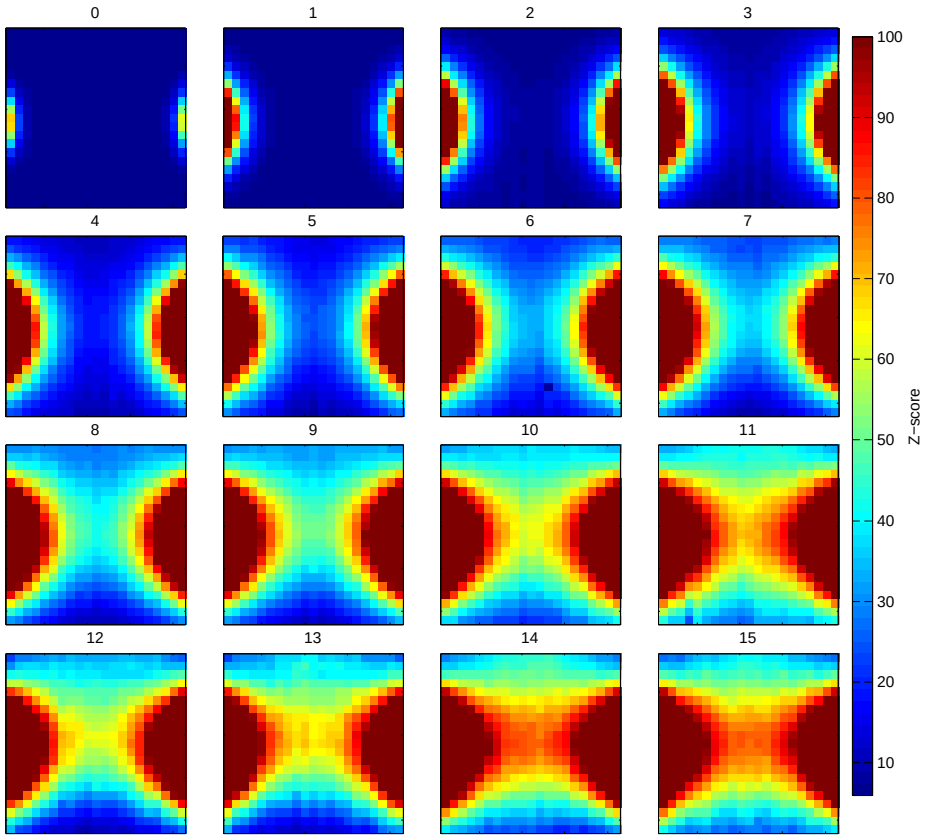

Figure 8. Z-scores map of size 21 x 21 points in the xz-plane in function of the current injection offset from 0 to 15. The maps should be interpreted in such a way that the higher is the z-score the stronger is the object visible on the image. The center of each image is electrode plane.

obtained results. A class 5 (error between 5 % and 10 %), the highest score in our sample tests, is achieved using offset larger than 3 and smaller than 14 and for hyperparameters 0.2, 0.02 and GREIT with noise figure equal to 0.5. We also showed that best z-score was expected when the electrode belt is placed at the same height as the target. We also recorded vertical cross-sectional maps of this effect.

The position precision was found to be an indicator for the object to be seen on the image. In this paper, we estimate that an object is visible in the image when the position precision is less than or equal to a threshold of 0.1. Since position precision is not an accessible metric in a clinical case, in which the ground truth image is not known, a surrogate is needed. In this respect, the correlation between the z-score and the position suggest that the former can be used as a possible surrogate. Nevertheless, further work is necessary in order to demonstrate the use of the z-score in a clinical setting for assessing the image reliability in term of medical interpretation.

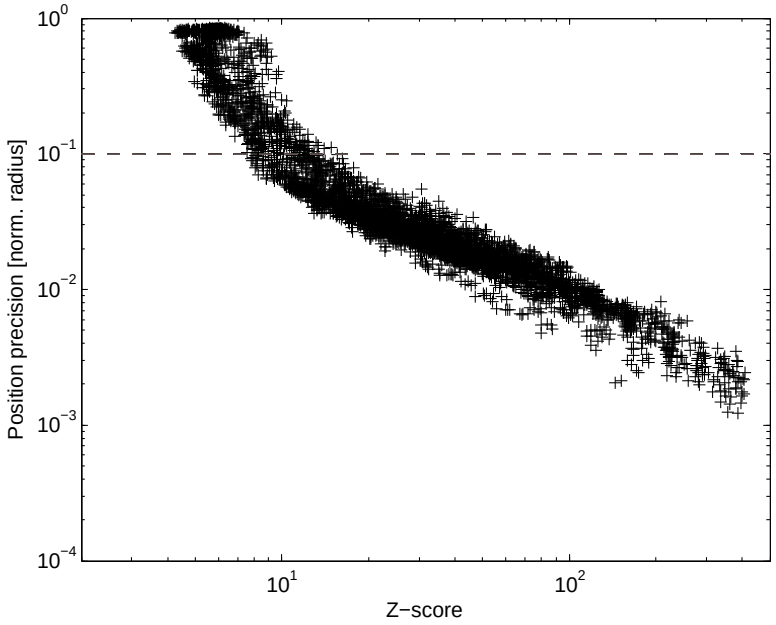

Figure 9. Z-scores versus position precision for offset from 0 to 10. The dotted line represents the postulated visibility limit for the test object.

The proposed error classes could be introduced into the specifications or data sheets of the various EIT systems making the documentation easier to read for the consumer. This could establish a common understanding of the performances of EIT devices. The proposed test procedures and image metrics are also easy to understand since they all rely on the comparison between the ground true position, shape and size of the test object and the same criterion derived from the obtained images.

Acknowledgment

We would like to acknowledge the Swiss Commission for Technology and Innovation (CTI: 12888.1 VOUCH-LS) and the company Swisstom AG for supporting this work.

References

[1] Gerhard K Wolf, Camille Gómez-Laberge, Jordan S Rettig, Sara O Vargas, Craig D Smallwood, Sanjay P Prabhu, Sally H Vitali, David Zurakowski, and John H Arnold. Mechanical ventilation guided by electrical impedance tomography in experimental acute lung injury. *Critical care medicine*, 41(5):1296–304, 2013.

[2] Andrea Borsic, Brad M Graham, Andy Adler, and William R B Lionheart. In vivo impedance imaging with total variation regularization. *IEEE transactions on medical imaging*, 29(1):44–54, 2010.

[3] H. Luoma-aho, P. Kauppinen, and R. Suuronen. *Sensitivity Distribution*

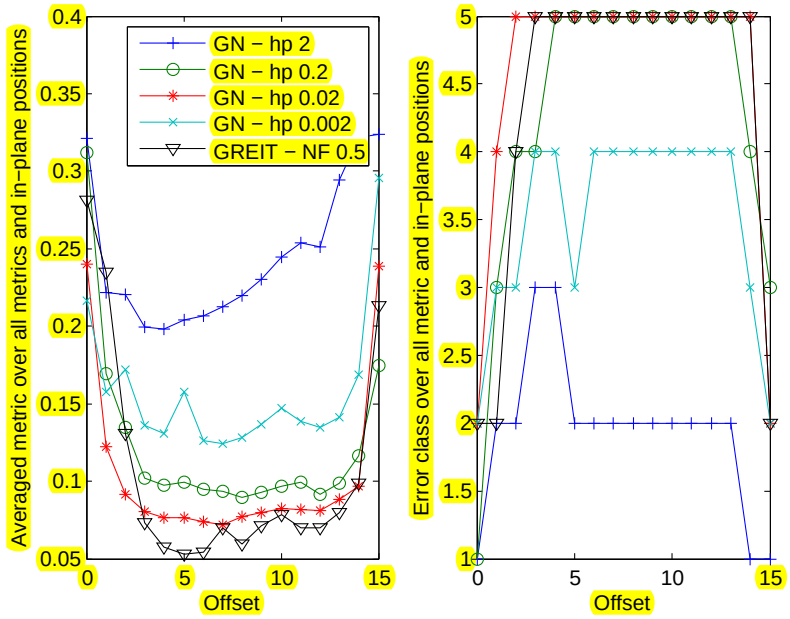

Figure 10. Error value and error classes averaged over all test object positions within the electrodes plane and over all four metrics. (left) averaged metric values, (right) ranking in error classes of the result presented on the left. The best averaged grade found here is 5.

Simulations of Electrode Configurations for Monitoring Tissue Grafts, pages 40–43. 2007.

[4] H Griffiths. A phantom for electrical impedance tomography. *Clinical Physics and Physiological Measurement*, 9 Suppl A(4 a):15–20, 1988.

[5] H Griffiths. A cole phantom for eit. *Physiological Measurement*, 16(3 Suppl A):A29–A38, 1995.

[6] G Hahn, M Beer, I Frerichs, T Dudykevych, T Schröder, and G Hellige. A simple method to check the dynamic performance of electrical impedance tomography systems. *Physiological Measurement*, 21(1):53–60, 2000.

[7] G Hahn, A Just, J Dittmar, and G Hellige. Systematic errors of eit systems determined by easily-scalable resistive phantoms. *Physiological Measurement*, 29(6):S163–S172, 2008.

[8] Hervé Gagnon, Martin Cousineau, Andy Adler, and Alzbeta E Hartinger. A resistive mesh phantom for assessing the performance of eit systems. *IEEE Transactions on Biomedical Engineering*, 57(9):2257–2266, 2010.

[9] Andy Adler and William R B Lionheart. Minimizing eit image artefacts from mesh variability in finite element models. *Physiological measurement*, 32(7):823–834, 2011.

[10] William R. B. Lionheart, Kyriakos Paridis, and Andy Adler. Resistor networks and transfer resistance matrices. *13th International Conference on Biomedical Applications of Electrical Impedance Tomography*, May 23-25 2012.

[11] Yasin Mamatjan, Stephan Boehm, Pascal O Gaggero, and Andy Adler. Evaluation of eit system performance. *Physiological Measurement*, 32(7):851–865, 2011.

[12] Iain Beardsell, Simon Bell, Helen Rumbold, and Sarah Robinson. *Get Through MCEM Part A: MCQs*. RSM Books, 2009.

[13] Pascal Olivier Gaggero, Andy Adler, Josef Brunner, and Peter Seitz. Electrical impedance tomography system based on active electrodes. *Physiological Measurement*, 33(5):831, 2012.

[14] Andy Adler, John Arnold, Richard Bayford, Andrea Borsic, Brian Brown, Paul Dixon, Theo Faes, Inez Frerichs, Herve Gagnon, Yvo Garber, and et al. Greit: towards a consensus eit algorithm for lung images. *Health San Francisco*, 2008.

[15] Andy Adler and Robert Guardo. Electrical impedance tomography: regularized imaging and contrast detection. *IEEE Transactions on Medical Imaging*, 15:170–179, 1996.

[16] M Soleimani, C Gomez-Laberge, and A Adler. Imaging of conductivity changes and electrode movement in eit. *Physiological Measurement*, 27(5):S103–S113, 2006.

[17] Andy Adler and William R B Lionheart. Uses and abuses of eidors: An extensible software base for eit. *Physiol. Meas.*, 27:S25–S42, 2006.

[18] Steve Eddins. Connected component labeling. blog.

[19] Andrew Adler, Pascal Olivier Gaggero, and Yasheng Maimaitijiang. Distinguishability in eit using a hypothesis-testing model. *Journal of Physics: Conference Series*, 224:012056, 2010.

[20] Pascal Olivier Gaggero. *Miniaturization and distinguishability limits of electrical impedence tomography for biomedical application*. PhD thesis, Université de Neuchâtel, 2011.